

---

# Ionospheric Sounding and Tomography by GNSS

---

Vyacheslav Kunitsyn, Elena Andreeva,  
Ivan Nesterov and Artem Padokhin

Additional information is available at the end of the chapter

<http://dx.doi.org/10.5772/54589>

---

## 1. Introduction

Studies of the ionosphere and the physics of the ionospheric processes rely on the knowledge of spatial distribution of the ionospheric plasma. Being the propagation medium for radio waves, the ionosphere significantly affects the performance of various navigation, location, and communication systems. Therefore, investigation into the structure of the ionosphere is of interest for many practical applications. Existing satellite navigation systems with corresponding ground receiving networks are suitable for sounding the ionosphere along different directions, and processing the data by tomographic methods, i.e. reconstructing the spatial distribution of the ionospheric electron density.

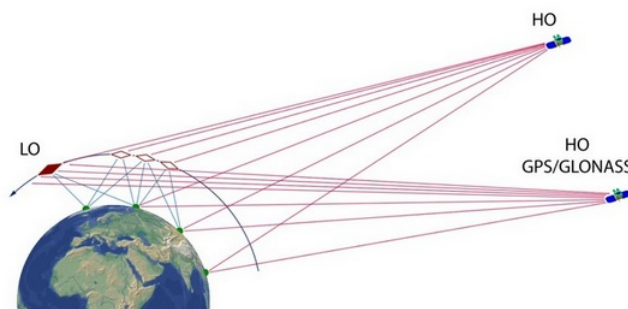


**Figure 1.** The geometry of the satellite radio sounding the near-Earth environment

In this Chapter, radio tomography (RT) methods based on low-Earth-orbiting (LO) and high-Earth-orbiting (HO) navigational satellites as well as radio occultation (RO) methods that use

the data of quasi tangential sounding are considered. The “old” LO navigational systems (American Transit and Russian Tsikada) allow the receivers to determine their locations everywhere on the Earth’s surface, but not continuously. The time gap between the neighboring positioning determinations depends on the number of operational satellites in orbit. The “new” HO systems (GPS/GLONASS) are suitable for continuous worldwide positioning measurements. As far as spatial coverage is concerned, all satellite navigation systems are global. They are further referred to here as the Global Navigation Satellite Systems (GNSS). Note that at present, the term GNSS is mainly applied to HO navigation systems (the American GPS and Russian GLONASS systems which are currently operational as well as European Galileo, Chinese BeiDou systems and Japanese QZSS).

Figure 1 depicts satellite radio probing of the near-Earth’s environment that includes the atmosphere, the ionosphere, and the protonosphere. Transmitters onboard the LO and HO satellites and the ground receivers provide the sets of rays intersecting the earth’s near-space and allow determining the group and phase paths of the radio signals (in the case of LO systems, only the phase paths) along the corresponding rays. The receivers onboard the LO satellites that receive the radio transmissions from the HO satellites are also suitable for determining the group and phase paths of the signal along the set of the rays that are quasi-tangential to the Earth’s surface. These measurements are suitable for sounding the near-space environment along various directions and calculating the integrals (or the differences of the integrals) of the refraction index in the medium. This set of integrals can be inverted by the RT procedure for the parameters of the medium. In the case of ionospheric sounding, the integrals of the refraction index are reduced to the integrals of the ionospheric electron density.

## 2. The methods of GNSS-based radio tomography

Methods of the satellite ionospheric radio tomography are being successfully developed at present [1-8]. Since the early 1990s, RT methods based on the LO navigation systems have been operational. In recent years, RT studies based on the measurements using HO navigation systems have been extensively conducted [6-8]. Further in the text, various types of radio tomography are referred to as low-orbital RT and high-orbital RT (LORT and HORT).

### 2.1. Low orbital ionospheric radio tomography

Present-day navigational systems are based on the low orbiting satellites flying in near-circular orbits at an altitude of about 1000-1150 km. These utilize chains of ground-based receivers, which capture RT data along different rays. In RT experiments, the phase difference between two coherent signals transmitted from the satellite at the frequencies of 150 and 400 MHz is recorded at a set of receiving stations on the ground. The receivers are arranged in a chain parallel to the ground projection of the satellite track, the distance between the neighboring receivers being typically a few hundred kilometers. The reduced phases  $\phi$  recorded at the receiving sites are the input data for the RT imaging. The integrals of the electron density  $N$

along the rays linking the ground receivers with the onboard satellite transmitter are proportional to the absolute (total) phase  $\Phi$  [1, 2], which includes the unknown initial phase  $\phi_0$ :

$$\alpha \lambda r_e \int N d\sigma = \Phi = \phi_0 + \phi \tag{1}$$

Here,  $\lambda$  is the wavelength of the satellite radio signal,  $d\sigma$  is the element of the ray, and  $r_e$  is the classical electron radius. The scaling coefficient  $\alpha$  (of the order of unity) depends on the sounding frequencies used. Equation (1) can be recast in the operator form [4] that includes the typical uncorrelated measurement noise  $\xi$ :

$$PN = \Phi + \xi \tag{2}$$

where  $P$  is the projection operator mapping the two-dimensional (2D) distribution  $N$  to the set of one-dimensional (1D) projections  $\Phi$ . Thus, the problem of tomographic inversion is reduced to the solution of the linear integral equations (2) for the electron concentration  $N$ . One of the probable ways to solve (2) is to discretize (approximate) the projection operator  $P$ . This yields the corresponding system of linear equations (SLE) with the discrete operator  $L$ :

$$LN = \Phi + \xi + E, E = LN - PN \tag{3}$$

where  $E$  is the approximation error that depends on the solution  $N$  itself. Note that equations (2) and (3) are equivalent if the approximation error  $E$  is known. However, in the case of reconstructing the data of a real RT experiment,  $E$  is not known, and, in fact, quite a different SLE is actually solved:

$$LN = \Phi + \xi \tag{4}$$

The system (4) is not equivalent to SLE (3). In other words, the difference between the solutions of (3) and (4) ensues from the difference in both the quasi-noise component and the correlated (in time and rays) approximation error  $E$ . For SLE (4) to be solved, the absolute phase  $\Phi$  together with  $\phi_0$  should be known. The errors in  $\phi_0$  estimated by the different receivers can result in the contradictory and inconsistent data, which leads to low-quality RT reconstructions. In order to avoid this difficulty, a method of phase-difference radio tomography (RT based on the difference of the linear integrals along the neighboring rays) was developed [9], which does not require the initial phase  $\phi_0$  to be determined. The SLE of the phase-difference RT is determined by the corresponding difference:

$$AN = LN - \dot{L}N = \Phi - \Phi' = D + \xi \tag{5}$$

where  $LN = \Phi$  is the initial SLE and  $L'N = \Phi'$  is the system of linear equations along the set of neighboring rays.

There are numerous algorithms, both direct and iterative, that solve SLEs (4) and (5). At present, in the problems of ray radio tomography of the ionosphere, iterative algorithms are most popular, although non-iterative algorithms are also used. These algorithms utilize a singular value decomposition with its modifications, regularization of the root mean square (RMS) deviation, orthogonal decomposition, maximum entropy, quadratic programming, Bayesian approach, etc. [3-7]. Extensive numerical modeling and LORT imaging of numerous experimental data revealed the efficient combinations of various methods and the algorithms that yield the best reconstructions.

“Phase-difference” LORT provide much better results and higher sensitivity compared to “phase only” methods. This is confirmed by reconstructions of the experimental data as well [4, 7]. The horizontal and vertical resolution of LORT in its linear formulation is 20-30 km and 30-40 km, respectively. If the refraction of the rays is taken into account, the spatial resolution of LORT can be improved to 10-20 km [7].

## 2.2. High orbital ionospheric radio tomography

Deployment of the global navigational systems (GPS and GLONASS) in USA and Russia offers the possibility to continuously measure trans-ionospheric radio signals and solve the inverse problem of radio sounding [6-8]. In the near future, there are plans to launch the European Galileo and Chinese BeiDou satellite systems. Signals of the present-day GPS/GLONASS are continuously recorded at the regional and global receiving networks (e.g., the network operated by the International GNSS Service, IGS, which comprises about of two thousand receivers). These data are suitable for reconstruction of the ionospheric electron density, the total electron content (TEC).

Inverse problems of radio sounding based on the GPS/GLONASS data, which pertain to the tomographic problems with incomplete data, are inherently high-dimensional. Due to the relatively low angular velocity of the high-orbiting satellites, allowance for the temporal variations of the ionosphere becomes essential. This makes the RT problem four-dimensional (three spatial coordinates and time) and exacerbates incompleteness of the data: every point in space is not necessarily traversed by the rays that link the satellites and the receivers, therefore the data gaps arise in the regions where only few receivers are available. The solution of this problem requires special approaches [10].

The methods of ionospheric sounding typically analyze the phases of the radio signals that propagate from the satellite to the ground receiver at two coherent multiple frequencies. For example, in the GPS-based soundings, these frequencies are  $f_1 = 1575.42$  MHz and  $f_2 = 1227.60$  MHz. The corresponding data ( $L_1$  and  $L_2$ ) are the phase paths of the radio signals measured in the units of the wavelengths of the sounding signal. Another parameter that can be used in the analysis is the pseudo-ranges (the group paths of the signals), which is the time taken by the wave-trains at the frequencies  $f_1$  and  $f_2$  to propagate from the source to the receiver. The

phase delays  $L_1$  and  $L_2$  are proportional to the total electron content, TEC, the integral of electron density along the ray between the satellite and the receiver:

$$TEC = \left( \frac{L_1}{f_1} - \frac{L_2}{f_2} \right) \frac{f_1^2 f_2^2}{f_1^2 - f_2^2} \frac{c}{K} + const, \tag{6}$$

where  $K = 40.308 \text{ m}^3\text{s}^{-2}$  and  $c = 3 \cdot 10^8 \text{ m/s}$  is the speed of light in vacuum. Note that, by using the phase delay data, it is only possible to calculate the TEC value up to a certain constant indicated as the additive term in formula (6). The relationship (6) is similar to formula (1) with the unknown constant in the right-hand side of the system.

TEC values can also be derived from the pseudo-ranges  $P_1$  and  $P_2$  [11]:

$$TEC = \frac{P_2 - P_1}{K \left( \frac{1}{f_2^2} - \frac{1}{f_1^2} \right)} \tag{7}$$

However, compared to phase data, the pseudo-range data are strongly distorted and contaminated by noise. The noise level in  $P_1$  and  $P_2$  is typically 20-30% and even higher, while in the phase data it is below 1% and rarely reaches a few percent. Therefore, for HORT, the phase data are preferable.

Most authors [6] solve the HORT problem using a set of linear integrals. In that approach, it is assumed that the TEC data are sufficiently accurately determined from the phase and group delay data (6, 7). However, the absolute TEC (7) is determined with a large uncertainty in contrast to the TEC differences that are calculated highly accurately. Therefore, the phase-difference approach was applied in this case, too [10, 12]. In other words, instead of the absolute TEC, its corresponding differences or the time derivatives  $dTEC/dt$  were used as input data for the RT problem.

The problem of the 4-D GNSS-based radio tomography can be solved by the approach developed in 2-D LORT. In this approach, the electron density distribution is represented in terms of a series expansion of the certain local basis functions; in this case, the set of the linear integrals or their differences is transformed into SLE. However, in contrast to 2-D LORT, here it is necessary to introduce an additional procedure interpolating the solutions in the area with missing data. The implementation of this approach in the regions covered by dense receiving networks (e.g., North America and Europe) with a rather coarse calculation grid and suitable splines of varying smoothness [10,12] has proved highly efficient.

Another approach seeks sufficiently smooth solutions of the problem so that the algorithms provide a good interpolation in the area with missing data. For example, let us consider a Sobolev norm and seek a solution that minimizes this norm over the infinite set of solutions of the initial (underdetermined) tomographic problem (5):

$$AN = D, \min_{AN=D} \|f - f_0\|_{W_n}^2 \quad (8)$$

Here, function  $f$  is the solution with a given weight .

Practical implementation of this approach faces difficulties associated with solution of the constrained minimization problem. The direct approach utilizing the method of Lagrange's undetermined multipliers gives SLE with high-dimensional (due to the great number of rays) matrices, which do not possess any special structure that would simplify the solution. Therefore, we solve this minimization problem by an iterative method [10] that is a version of the SIRT technique, with additional smoothing (by filtering) of iterative increments over the spatial variables. This method allows for use of a-priori information that can be introduced both through the initial approximation for the iterations and through weighting coefficients that determine the relative intensity of electron density variations at different heights.

Computer-aided modeling shows that quasi-stationary ionospheric structures can be reconstructed with reasonable accuracy, although HORT has a significantly lower resolution than LORT. As a rule, the vertical and horizontal resolution of HORT is 100 km at best, and the time step (the interval between two consecutive reconstructions) is typically 20 - 60 minutes. In regions covered by dense receiving networks (Europe, USA, and Alaska), the resolution can be improved to 30-50 km with a 10 - 30 minute interval between consecutive reconstructions. Resolution of 10-30 km with a time step of 2 minutes can only be achieved in the regions with very dense receiving networks (California and Japan).

### 3. Testing and validation of ionospheric radio tomography

In numerous experiments, RT images of the ionosphere have been compared with corresponding parameters (vertical profiles of electron density and critical frequencies) measured by ionosondes [13-18, 4, 19, 7]. In most cases, the RT results closely agree with ionosonde data within the limitations of the accuracy of both methods. An example of such a comparison with the world's first RT reconstruction of an ionospheric trough is presented in Figure 2. Here, the dots show the vertical profile of electron density according to measurements by an ionosonde in Moscow, and the solid line displays the corresponding profile calculated from the RT reconstruction for April 7, 1990 (22:05 LT).

A comparison of a few hundred ionospheric RT cross-sections in the region of the equatorial anomaly with observations by two ionosondes in October-November 1994 [19] is illustrated in Figure 3. The distributions of electron density were reconstructed from RT measurements at the low-latitude Manila-Shanghai chain, which included six receivers arranged along the meridian  $121.1 \pm 1^\circ\text{E}$  within the latitude band between  $14.6^\circ\text{N}$  and  $31.3^\circ\text{N}$ . One ionosonde was installed at  $25.0^\circ\text{N}$ ,  $121.2^\circ\text{E}$  7.5 km of Chungli almost in the middle of the chain. Another ionospheric station was located in the southernmost part of the chain in Manila ( $14.7^\circ\text{N}$ ,  $121.1^\circ\text{E}$ ).

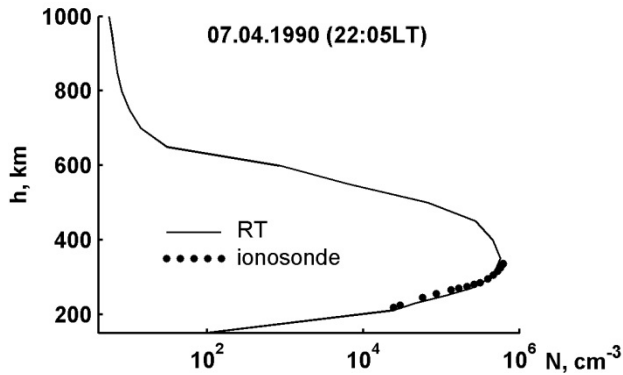


**Figure 2.** Vertical profiles of electron density in Moscow at 22:05 LT on April 7, 1990, depicting both radio tomography and ionosonde data.

Using RT reconstructions, maximal electron densities and plasma frequencies  $f_0F2$  were calculated in the vicinities of the ionospheric stations. These parameters were then compared to the corresponding values determined from ionosonde measurements. These two data sets are compared in Figure 3. The points that lie on the bisectrix of the right angle correspond to the case where the RT-based and the ionosonde-based critical frequencies exactly coincide. We also calculated the normalized root mean square (rms) deviations of the RT-based critical frequencies  $f_0F2$  from the corresponding values inferred from the ionosonde measurements.

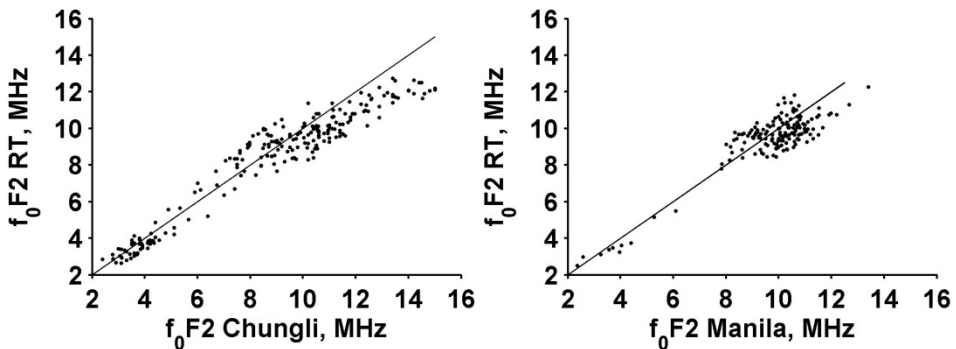


**Figure 3.** The comparison between the plasma frequencies  $f_0F2$  calculated from the RT reconstructions and the corresponding values derived from the measurements by the ionosondes in (left) Chungli and (right) Manila for October–November 1994.

A detailed analysis reveals the following points.

1. The scatter in  $f_oF2$  in Chungli is larger than in Manila. The normalized rms deviations for the ionosondes in Chungli and Manila are 11.2% and 8.9%, respectively.
2. In the case of high electron concentrations, especially for  $f_oF2$  above 13 MHz, the experimental points tend to saturation: the critical frequencies  $f_oF2$  derived from RT fall short of the corresponding values calculated from the ionosonde measurements.

These features indicate that strong spatial gradients in electron density typical in the region of the equatorial anomaly can cause the discrepancies in the plasma frequencies calculated from RT and ionosonde measurements.

In experiments on vertical pulsed sounding of the ionosphere, the signal is not reflected from directly overhead. Even in the case of vertical sounding of a horizontally stratified ionosphere, the ordinary wave tends to deviate toward the pole, and in the point of reflection, it becomes perpendicular to the local geomagnetic field [20]. Therefore, in the general case, reflection does not occur vertically above the sounding point but somewhat away from overhead.

Zero offsets are only observed at the equator, while in the region of the Chungli ionosonde, the offset can be  $\sim 10$  km. In addition, Chungli is located close to the maximum of the equatorial anomaly, which is marked by very strong gradients. Therefore, the sounding ray of the Chungli ionosonde will significantly deflect before having been reflected backwards. Therefore, the values of  $f_oF2$  recorded by the Chungli ionosonde will by no means be the actual  $f_oF2$  values exactly overhead. These considerations will help us to interpret the results of comparison of plasma frequencies.

First, at high plasma frequencies ( $f_oF2$  higher than 13 MHz), the experimental points in Figure 3 fall below the bisectrix. This area relates to the stage of a completely mature anomaly with a well-developed crest and, therefore, with strong gradients in electron density. It is due to these gradients that the values of  $f_oF2$  determined from the ionosondes are, on average, overestimated compared to the actual critical frequencies  $f_oF2$  overhead.

Second, values of  $f_oF2$  at Chungli demonstrate a larger scatter than at Manila. Since Chungli is located in the central part of the RT chain, the most reliable RT reconstructions are expected at the latitudes near the middle segment of the chain (close to Chungli) rather than on its margins (Manila). This contradicts the actual results shown in Figure 3. On the other hand, Chungli is located in the vicinity of the peak electron density within the crest of the anomaly, in the area of strong gradients, where errors of vertical sounding (associated with deflection of the reflected ray) are most probable. Therefore, large discrepancies in the Chungli region are quite probable, which is confirmed by Figure 3.

It is worth noting that the ionosonde measurements during geomagnetically disturbed periods are often unstable because the ionosphere experiences significant transformations that alter the radio propagation conditions. In particular, the electron density  $N$  in the  $D$ -region ionosphere sharply increases, and, due to strong radio absorption, most ionograms do not show any reflections. The examples in Figures 4 and 5 illustrate a comparison of the critical frequencies calculated from the phase-difference RT reconstructions above the Cordova-Gakona-Delta chain in Alaska with those derived from ionosonde measurements in Gakona during the

geomagnetic storms in October 2003 (Figure 4) and June 2004 (Figure 5). The interval from October 29 to 31, 2003 was marked by the strongest recorded geomagnetic storm. During the main phase of the storm, the 3-h  $K_p$  index attained its maximum possible value (9). Figure 4 shows that the ionosonde data are fragmentary and, starting from October 28, 2003 (13:00UT) through October 31, 2003 (19:30 UT), i.e., exactly during the peak of the geomagnetic storm, they are missing altogether. The ionosonde observations at Gakona are discontinuous during the geomagnetically disturbed period in July 2004 ( $K_p = 8$  and  $K_p = 7$  on July 25 and July 27, respectively). On some days, the reflections are almost absent (e.g., from July 23 through July 27). In contrast to the ionosondes, which are essentially HF radars, RT methods continue to be suitable for imaging the ionosphere even during strongly disturbed solar and geophysical conditions, because the high sounding frequency used in RT applications (150 MHz) allows one to neglect the absorption.

Comparison of the RT results with ionosonde data can only be implemented in terms of critical frequencies or vertical profiles of electron density up to the ionospheric peak height and only for points located close to the ionosondes. In other words, the single-point ionosonde measurements cannot be inverted into the two-dimensional (2D) ionospheric cross sections. Therefore, it is of particular interest to compare RT images with measurements by incoherent scatter (IS) radars, which are also suitable for reconstructing 2-D cross-sections of the ionosphere over an interval of a few hundred kilometers.

Pryse and Kersley [21] made a preliminary attempt to compare the ionospheric cross-section derived from measurements by two receivers with EISCAT IS radar data in Tromso (Norway). The RT reconstructions coarsely reproduced the horizontal gradient in electron density determined from the EISCAT. Since that work, the results of these two independent methods of the ionospheric research, namely, RT and IS radar measurements, have been intercompared for numerous RT experiments [22-25, 15, 26-28].

Below, we present the results of the Russian-American Tomography Experiment (RATE'93) carried out in 1993. RATE'93 was one of the first experiments in which RT images of the ionosphere were intercompared with IS data measured by the Millstone Hill radar (USA). The idea of this experiment was suggested by the American geophysicists from the Haystack Observatory and Philips Laboratory. The Russian team included scientists from the Polar Geophysical Institute and Moscow State University [24]. Four mid-latitude RT receiving sites were arranged along the 288°E meridian in the northeastern USA and in Canada (Block Island (41.17°N), Nashua, NH (42.47°N), Jay, VT (44.93°N), and Roberval, Canada (48.42°N)).

Each receiving site was equipped with the Russian receivers, which recorded the signals of the Russian navigational satellites like Tsikada, and the receivers designed at the Philips Laboratory, which measured radio transmissions from the Transit satellites of the Navy Navigation Satellite System (NNSS). The IS radar at the Haystack observatory in Millstone Hill (42.6°N, 288.5°E) scanned the ionosphere in the latitude-height plane in a coordinated mode with RT observations. The Russian team reconstructed the distributions of the ionospheric electron density using the "phase-difference" approach while the American geophysicists used the "phase" RT method.

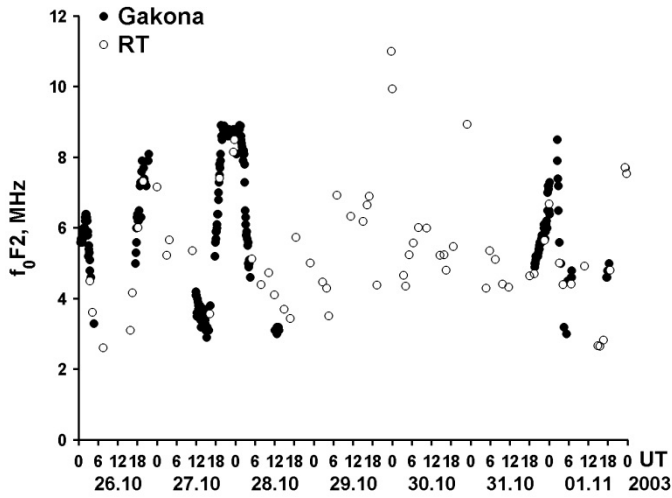


**Figure 4.** The comparison of the critical frequencies  $f_0F2$  derived from the RT reconstructions and from the ionosonde measurements at Gakona during severe solar-geomagnetic disturbances from October 26 to November 1, 2003.

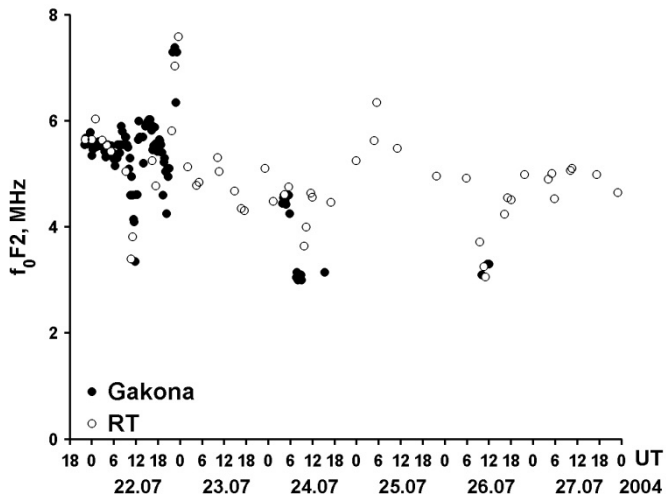


**Figure 5.** The comparison of the critical frequencies  $f_0F2$  derived from the RT reconstructions and from the ionosonde measurements at Gakona during the geomagnetic and ionospheric disturbances from July 22 to July 27, 2004.

In this experiment, not only were the RT results compared with the IS radar data, but also the two different RT approaches (phase-difference and phase techniques) were assessed. The time of the experiment was chosen to coincide with expected solar activity [29]. A strong geomagnetic storm occurred between November 3 and 4, 1993. During this storm, the  $A_p$  index of

planetary geomagnetic activity reached 111 nT, and during the main phase of the storm, the 3-h Kp index was 6.7.

The results of RATE'93 demonstrated the high quality of the RT ionospheric cross-sections reconstructed by the phase difference method [24]. It should be noted that RT cross-sections and radar ionospheric images are clearly similar in the case of a smooth, almost regular ionosphere with insignificant local extrema. Further in the text, the results are visualized in the coordinates "height  $h$  above the Earth's surface (in km) - latitude." Figure 6 presents the cross-sections of the ionosphere about 1 hour 45 minutes after the sudden storm commencement (at 23:00 UT on November 3, 1993). The ionospheric cross-section based on the IS radar data is displayed in Figure 6 (upper panel), and the phase-difference RT reconstruction is shown in Figure 6 (lower panel).

A characteristic trough appeared about 44°N, and the ionization sharply increased in the height interval from 200 km to 300 km near 47°N, due to precipitation of low-energy particles between 46°N and 51°N [29]. Figure 6 shows that the RT cross-section closely agrees with the radar ionospheric image. However, it should be noted that radar measurements are limited to the height interval from 180 km (below which the concentrations are insignificant) to 600 km (above which the distortions and noise level are very high) [29].

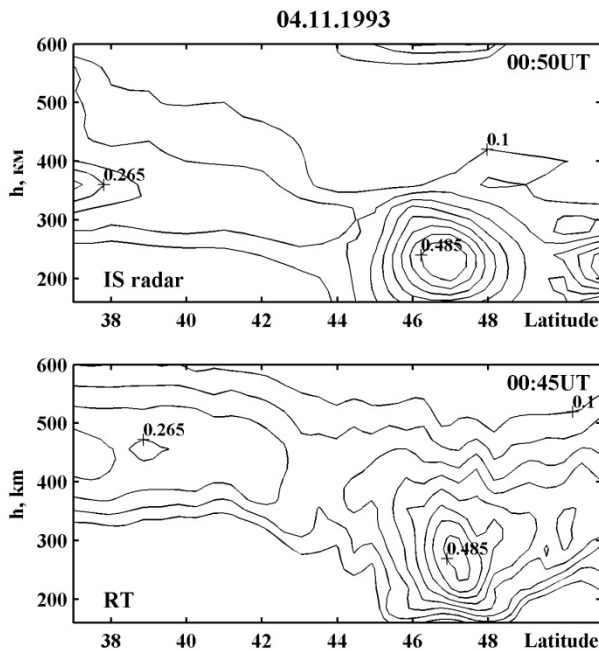
The similarity of the RT cross-sections and radar ionospheric images (Figure 6) confirms that the increase in the radar signal in the bottom  $F$ -region ionosphere reflects the actual enhancement of electron density substantially below 300 km, but not the noise or coherent backscatter from the irregularities associated with the  $E$ -region electric fields [24, 29]. Moreover, both ionospheric cross-sections in Figure 6 clearly demonstrate the elevated  $F$ -region south of 45°N. The elevation increases with increasing distance to the trough. The elevation in the RT reconstruction attains 400-450 km and is larger than in the radar image.

Figure 6 (upper panel) shows the preliminary radar-based ionospheric cross-section as published in [24]. The difference between the reconstructions is 32.6%, which falls within the accuracy of both methods. However, it should be noted that the ionospheric cross-sections based on radar data and those reconstructed from the RT measurements do not correspond to the same time interval but are somewhat spaced in time. The time shift between them is 5 minutes, which is quite a significant value considering that the measurements were conducted during the period of active structural rearrangement of the ionosphere on November 4, 1993.

In their later paper, Foster and Rich [29] quote the final radar cross section that was reconstructed after scrupulous analysis of the measurements. On that image, the bottom of the ionospheric  $F$ -layer is observed at the same height as in the RT image shown in Figure 6 (lower panel), i.e., at 400-450 km. According to the radar data, the  $F$ -layer remained elevated for a short lapse of time (~20 minutes).

In this experiment, a narrow (<2°) tilted trough was detected by both RT and radar observations at a latitude of 41°-42° at 04:56UT on November 4, 1993. Phase-difference tomography also revealed a border about 50 km in size on the northern wall of the trough, which has not been distinguished by the radar observations [24]. This means that the phase-difference RT method has higher horizontal resolution. The border clearly manifests itself in the phase of

the signal recorded at the Nashua receiving site (Figure 7), where it produces a local maximum at about  $41.5^{\circ}$ - $42^{\circ}$ N. In contrast to the phase-difference RT, all the ionospheric images reconstructed by the phase RT are similar to each other and close to the PIM model [30]. Due to errors in the determination of the initial phases, the phase RT method does not even reveal the troughs themselves. The comparison shows that the cross-sections of electron density reconstructed by the phase-difference RT and the ionospheric images derived from the IS radar data agree within the accuracy of both methods. Moreover, compared to the IS method, phase-difference RT has a higher horizontal resolution. However, the IS radar revealed thin (<50 km) extended horizontal layers which are not resolved by radio tomography due to the insufficient base of the RT measurements (the distance between the outermost receivers in the experiment was only 800 km) and a quasi-tangential (to the Earth's surface) rays were absent.



**Figure 6.** Cross sections of the ionosphere after sudden commencement of the geomagnetic storm (00:45 UT on November 4, 1993): (a) according to the radar data; (b) according to phase-difference RT.

This experiment also demonstrated that the method of phase-difference RT has noticeable advantages (in sensitivity and quality of the reconstructions) over the phase radio tomography which uses linear integrals. A comprehensive intercomparison between the results of phase tomography, phase-difference tomography, and IS radar studies is presented in the final summarizing paper [24].

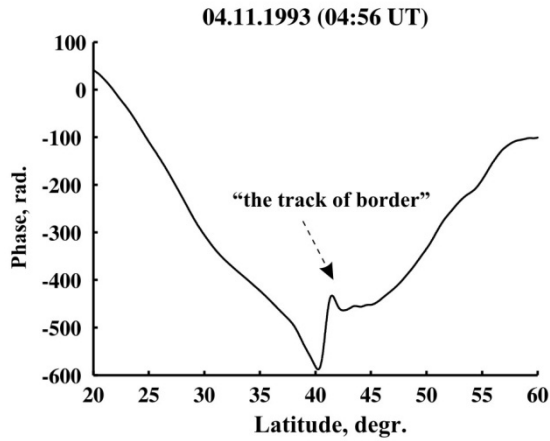


Figure 7. Phase of the satellite radio signal recorded at Nashua at 04:56 UT on November 4, 1993

Numerous comparisons have been carried out between the HORT results and the ionospheric measurements in Europe, Russia, America, and Southeast Asia. The diurnal behavior of critical frequencies derived from the HORT data quite closely agrees with the ionosonde data. Figures 8-9 present examples of a comparison of HORT-based critical frequencies with ionosonde measurements at Rome, Tromso, and Boulder during the disturbed period on March 9, 2012, when the Kp index reached 7. A similar comparison for Yamagawa is presented for the mega-earthquake in Japan. During geomagnetically quiet periods, discrepancies between the critical frequencies are typically far below 1 MHz.

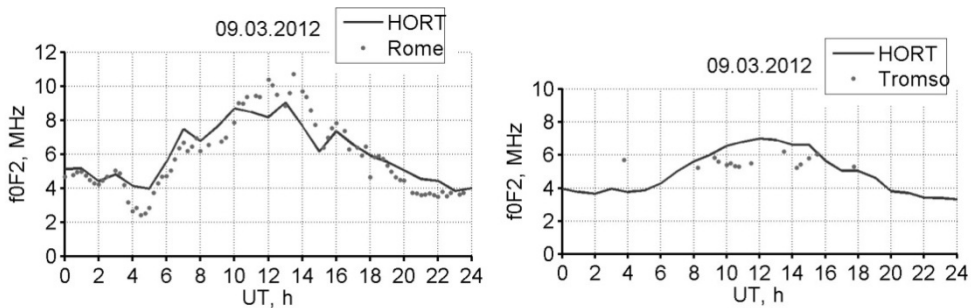
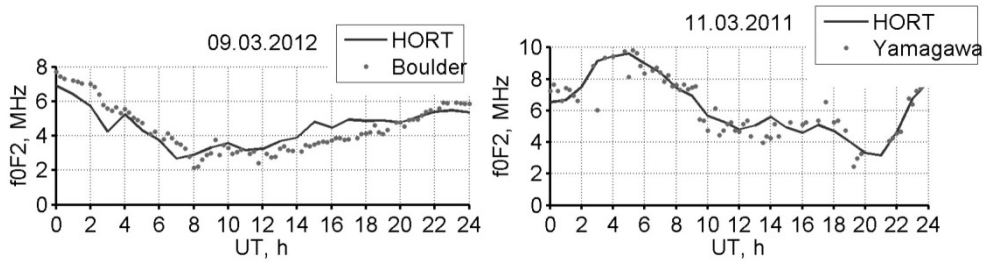


Figure 8. The comparison the HORT-based critical frequencies with the ionosonde measurements at Rome (left) and Tromso (right)

During severe geomagnetic disturbances, the RMS deviation of critical frequencies is about 1 MHz. These comparisons were carried out using data containing a few thousand samples. For example, for the interval of the strong Halloween storm from October 29 to November 1,

2003, with measurements from 13 North American ionosondes, the RMS deviation of the critical frequencies was 1.7 MHz [31].



**Figure 9.** Comparison of HORT-based critical frequencies with ionosonde measurements at Boulder (left) and Yamagawa (right)

#### 4. Examples of the GNSS-based ionospheric radio tomography

The world's first LORT images were reconstructed in March-April 1990 by geophysicists of the Moscow State University and Polar Geophysical Institute of the Russian Academy of Sciences [32]. One of the first RT cross sections of the ionosphere between Moscow and Murmansk is presented in Figure 10. The horizontal axis in this plot shows the latitudes, and the vertical axis, the heights. The ionospheric electron density is given in units of  $10^{12} \text{ m}^3$ . This image clearly shows a proto-typical ionospheric trough at about  $63^\circ$ – $65^\circ\text{N}$  and a local extremum within it. Further experiments revealed the complex and diverse structure and dynamics of the ionospheric trough [1-8]. In 1992, preliminary results in RT imaging of the ionosphere were obtained by colleagues from the UK [21]. The LORT-based studies and applications drew significant interest from geophysicists around the globe. At the present time, more than ten research teams in different countries are engaged in these investigations [3-7]. Series of LORT experiments carried out in Europe, America, and Southeast Asia during the last twenty years [3-8] have demonstrated the high efficiency of radio tomographic methods for study of diverse ionospheric structures.

Quite often, RT images of the ionosphere in different regions reveal the well-known wave structures - traveling ionospheric disturbances (TID). The example in Figure 11 depicts an RT ionospheric image with distinct TIDs having a typical slope of  $45^\circ$ , as recorded on the Moscow-Arkhangelsk RT link [33]. Here, the ionosphere is quite moderately modulated by the TIDs (the modulation depth is 25-30%). Such TIDs are often observed in RT reconstructions, as mentioned in [5, 34].

RT experiments in Southeast Asia at the low-latitude Manila-Shanghai chain revealed a series of characteristic features in the structure of the equatorial anomaly (EA) including the post-noon alignment of the mature core of the EA (the area close to the peak electron concentration)

along the magnetic field axis; the significant asymmetry of the EA flanks, and the specific alteration of the thicker and thinner segments of the ionospheric *F*-layer [35, 19, 36]. The stable structural features of the EA observed in the RT experiments can be interpreted by analyzing ionospheric plasma flows and velocities in the region of the EA, which are caused by the fountain effect [7, 20, 35].

Imaging the *E*-region ionosphere by LORT methods is a far more difficult problem, because the contribution of the *E*-layer in the RT input is noticeably smaller than the contribution of the *F*-layer. However, if the size and geometry of the RT observation system are favorable for constructing a set of the rays that intersect the ionospheric *F*- and *E*-layers, it is possible to image the distribution of electron density in the *E*-layer [37]. An example of the LORT reconstruction of the *F*- and *E*-layers in the EA region is presented in Figure 12. The geomagnetic field lines are shown by the dashes. The mature core of the anomaly is oriented along the geomagnetic field; the edges of the EA crest are clearly asymmetric, and the thickness of the *F*-layer experiences distinct variations. The bottom side *F*-layer sags down due to the field-aligned plasma stream, i.e. the ionospheric plasma from the *F*-region penetrates down into the lower part of the *E*-layer in the interval of 24°-26°N. A constriction (“isthmus”) is formed in the area beyond the core of the anomaly (~ 28°-31°).

Today, more than a dozen LORT receiving networks (chains) are currently operational in different regions of the world (in Russia, contiguous United States and Alaska, Great Britain, Scandinavia and Finland, Greenland, Japan, and the Caribbean region [2-8]), which are extensively used for research and scientific studies. A new LORT system has been built in India, and the LORT system in Southeast Asia is being upgraded. The Russian transcontinental LORT chain includes nine receiving sites arranged along the Sochi-Moscow-Svalbard line. It is the world's longest LORT chain (about 4000 km in length) [38]. This chain is unique in the fact that its measurements cover a huge ionospheric sector stretching from the polar cap and auroral regions to the low latitudes. Due to this, measurements on this chain are suitable for studying the transfer of the disturbances between the auroral, subauroral, and low-latitude ionosphere, and for investigating the structure of the ionospheric plasma in different latitudinal regions as a function of solar, geophysical, and seasonal conditions. The Russian RT chain and the receiving RT chain in Alaska are located on the opposite sides of the Earth with a 12-hour time shift between them.

Various waves and wavelike structures are another specific feature often observed in LORT reconstructions. Figure 13 presents an example of a complex wave-like perturbation with a distinctive wave-front which was observed during the Halloween storm of 2003 in the Alaska region. A similar structure was also detected above the Russian LORT system (Moscow-Svalbard) during the geomagnetic storm in July, 2004 [7]. It is worth noting that the ionospheric plasma can be highly complex in its structure even in undisturbed conditions. This is illustrated by Figure 14 which shows the LORT cross section of the ionosphere between Sochi and Svalbard during geomagnetically quiet conditions ( $K_p < 1$ ). Wavelike disturbances with a characteristic size of 50 km are seen above Svalbard (78°-79°N). In the central segment of the image (59°-65°N) the electron density decreases. In the southern part of the cross-section (42°-55°N), wavelike structures with a spatial period of 100-150 km are apparent. A wide

ionization trough in the interval of 62°-64°N is observed on the LORT reconstruction in Figure 15. The local maximum at 65°-66°N is almost merged with the polar wall of the trough. A spot of enhanced ionization is identified within the trough about 63°-64°N latitude. And, wavelike disturbances are revealed throughout 66°-78°N.

Besides being suitable for reconstructing the large-scale ionospheric phenomena of natural origin, LORT is also efficient for tracking artificial ionospheric disturbances. The LORT cross-section in Figure 16 shows wavelike structures that formed in the ionosphere within 30 minutes after launch of a rocket from the Plesetsk Cosmodrome. The cosmodrome is located approximately 63°N (200 km) distant from the satellite ground track. These anthropomorphic disturbances have a very complex structure wherein large irregularities (200-400 km) coexist with smaller ionospheric features (50-70 km), and the slope of the "wavefront" is also varying. Wave disturbances generated by launching high-power rocket vehicles are described in [39] where it is shown that ignition of the rocket generates acoustic-gravity waves (AGW) which, in turn, induce corresponding perturbations in electron density. During RT experiments with the Moscow-Murmansk chain, long-lived local disturbances in the ionospheric plasma were also identified above sites where ground industrial explosions were carried out [40].

RT methods revealed generation of ionospheric disturbances by the Sura ionospheric heating facility, which radiated high-power HF waves, modulated with a 10-minute heat/off cycles [41]. Figure 17 shows an ionospheric cross-section through a typical heated area. A narrow trough in the ionization, aligned with the propagation direction of the heating HF wave, is identified. Traveling ionospheric disturbances associated with the acoustic gravity waves (AGWs) generated by the Sura heater are observed diverging from the heated area. Unfortunately, insufficient density of HO receivers in central Russia prevented us from obtaining high-quality HORT images of the ionosphere during this heating experiment; however, the data recorded by the few available receivers support presence of the AGWs [41].

Thus, LORT is capable of reconstructing nearly instantaneous 2-D snapshots of the electron density distribution in the ionosphere (which actually cover a time span of 5-15 minutes). The time interval between the successive RT reconstructions depends on the number of the operational satellites and, as of now is 30-120 minutes. The LORT method is also suitable for determining plasma flows by analyzing successive RT cross sections of the ionosphere [42]. An optimal LORT receiving system, consisting of several parallel chains located within a few hundred km of each other, would allow 3-D imaging of the ionosphere. The requirement for multiple receiving chains is the major limitation of LORT.

The reconstructions presented below illustrate the possibilities of newly developed HORT techniques. Figure 18 displays the evolution of the ionospheric trough above Europe in the evening on April 17, 2003. The TEC maps and the meridional cross sections along 21°E show the trough widening against the background, with an overall nighttime decrease in electron density.

Figure 19 shows anomalous increases in electron density (up to  $3 \cdot 10^{12} \text{ m}^{-3}$ ) above the Arctic during the severe Halloween geomagnetic storm on October 29-31, 2003. The spots of increased electron density in the night sector are associated with the ionospheric plasma entrained by the anti-sunward convection stream from the dayside ionosphere. These areas with increased electron density are shaped as tongues with a patchy structure (upper panels), which can also be seen on the vertical cross sections (lower panels). The cross-sections cut the ionosphere along the lines indicated on the TEC maps. This spatial distribution of ionospheric plasma is a result of ionospheric plasma instabilities and the formation of wavelike disturbances. An example of imaging the Arctic ionosphere on December 16, 2006 is presented in Figure 20. Here, a characteristic ring-shaped structure encircles the pole, which is associated with convection and entrainment of ionospheric plasma from the dayside ionosphere into the night-side sector. Similar ring structures were observed in modeling of the Arctic ionosphere [43, 44].

Data recorded at the European GPS receiving network were used for imaging the ionosphere above Western Europe during the strong geomagnetic storm on October 28-31, 2003. The vertical TEC calculated from HORT reconstructions from 23:00 UT on October 30 to 02:00 UT on October 31 during the main phase of the storm are shown in Figures 21 and 22 as TECU isolines. During that time, the region was dominated by enhanced ionization. The electron density in the central part of the spot of increased ionization ( $(1.5-2) \cdot 10^{12} \text{ m}^{-3}$ ) significantly exceeds typical daytime values. The size of the spot (at half-maximum VTEC) is about 1500-2000 km in the north-to-south direction and 2500-3000 km in the west-to-east direction. The spot is seen moving from west to east with a southward component.

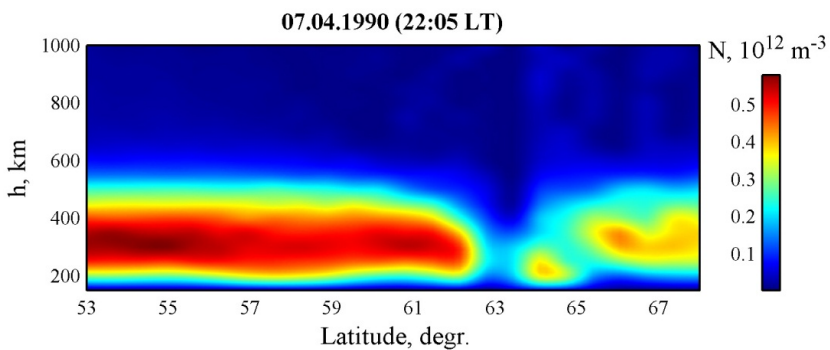


**Figure 10.** LORT image of the ionosphere (Moscow-Murmansk) on April 7, 1990 at 22:05 LT

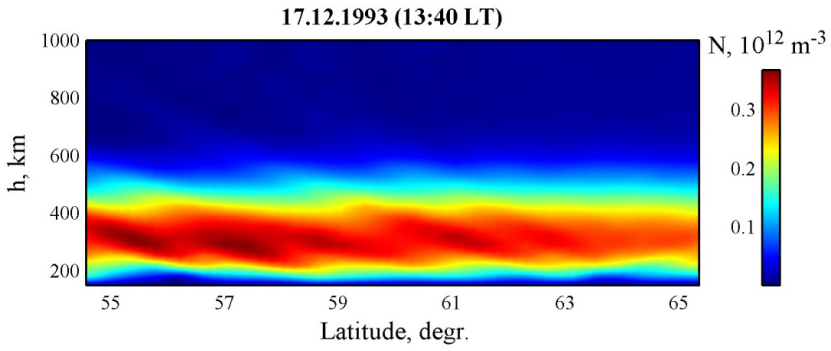


Figure 11. LORT image of the ionosphere (Moscow-Arkhangelsk) on December 17, 1993 at 13:40 LT

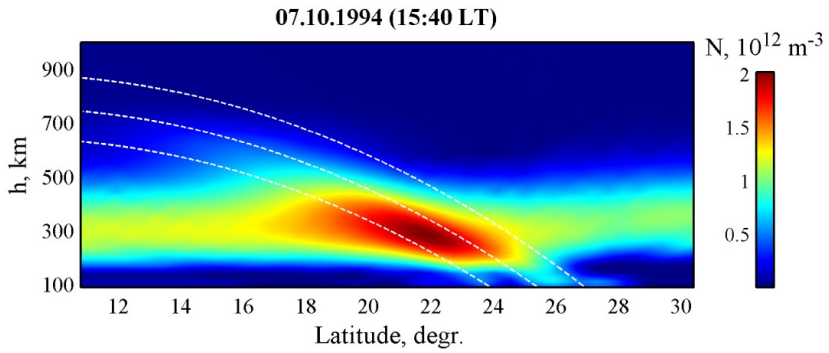


Figure 12. LORT image above Manila-Shanghai on October 7, 1994 at 15:40 LT

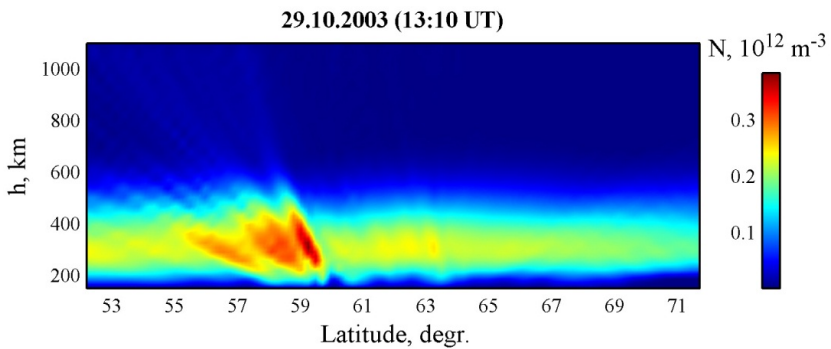
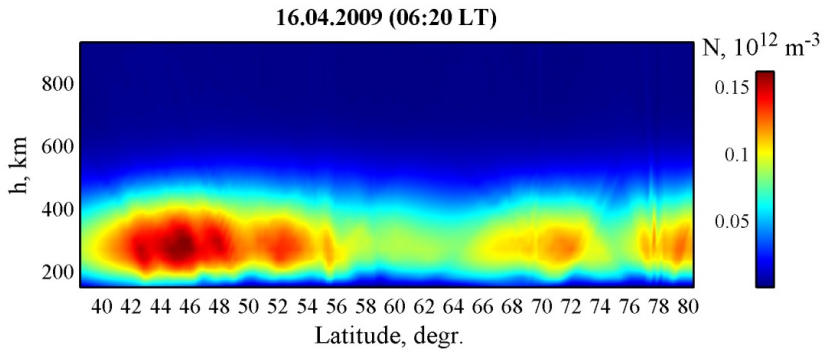
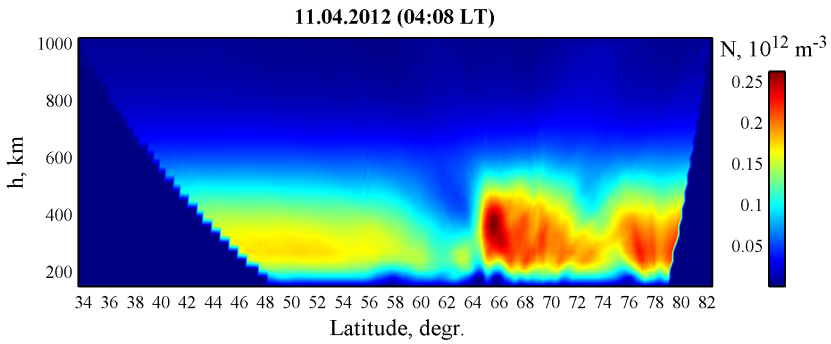


Figure 13. LORT image of the ionosphere above Alaska region on October 29, 2003 at 13:10 UT



**Figure 14.** LORT image of the ionosphere (Sochi-Svalbard) on April 16, 2009 at 06:20 LT



**Figure 15.** LORT image of the ionosphere (Moscow-Svalbard) on April 11, 2012 at 04:08 LT

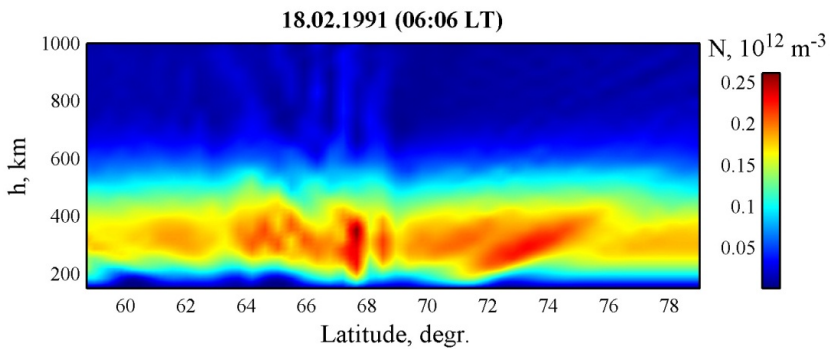


**Figure 16.** LORT image of the ionosphere (Moscow-Murmansk) on December 18, 1991 at 06:06 LT

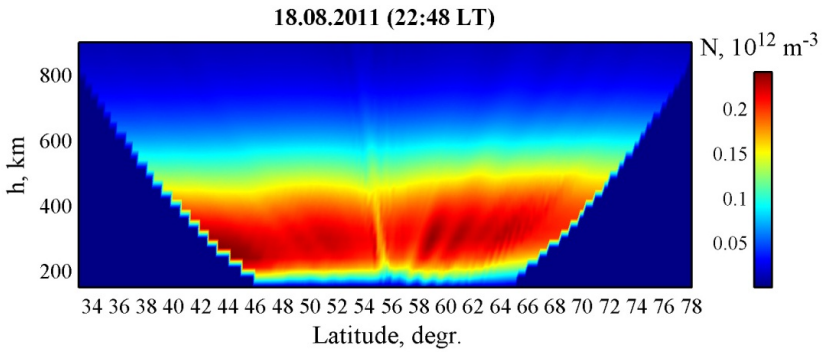


**Figure 17.** LORT-image of the ionosphere above Sura heating facility on August 18, 2011 at 22:48 LT

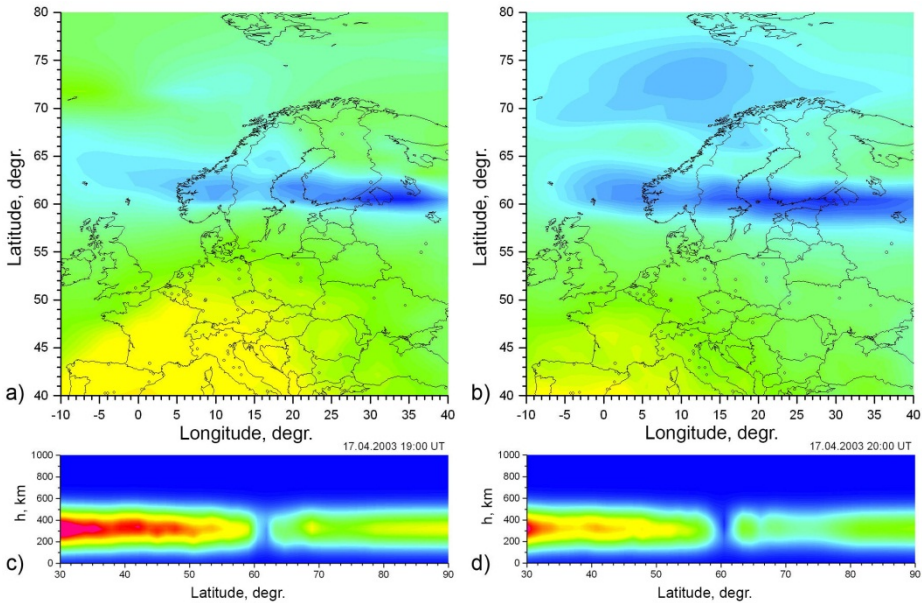


**Figure 18.** Ionospheric HORT reconstructions over Europe on April 17, 2003: (a, c) 19:00 UT, (b, d) 20:00 UT. (a, b): TEC maps in the latitude-longitude coordinates; the color scale is from 0 to 35 TECU (1 TECU= $10^{16}$  m<sup>-2</sup>). (c, d): Meridional cross sections along 21°E in the latitude-altitude coordinates; the color scale is from 0 to  $0.6 \cdot 10^{12}$  m<sup>-3</sup>

The LORT reconstruction above at the Russian chain (Moscow-Murmansk) reveals a variegated multi-extremal distribution of electron density during the night of 30/31 October ( $K_p = 9$ ). A spot of enhanced ionization attaining  $1.5 \cdot 10^{12} \text{m}^{-3}$  (which is a typical value for the equatorial anomaly), is observed at 70°-72°N (Figure 23). This spot is probably a result of the anti-sunward ionospheric convection combined with low-energy particle precipitation. Global

two-cell ionospheric convection is responsible for formation of the tongues of ionization (TOI), which are fragments of the low- and mid-latitude dayside ionospheric plasma entrained through the cusp and polar cap into the night-side ionosphere and distributed along the night-side of the auroral oval. The TOI is associated with the spots of the increased ionization drifting from the north southwards and from the east westwards [45].

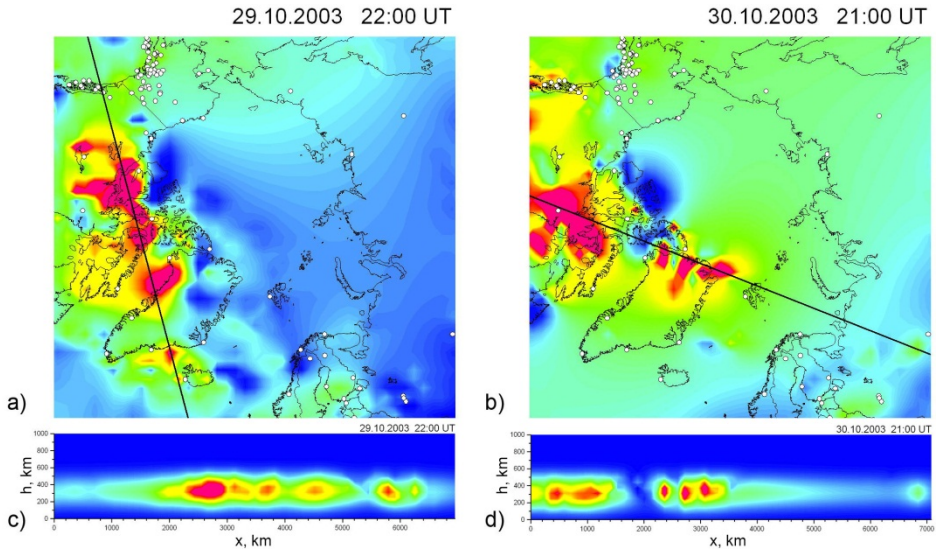


**Figure 19.** HORT reconstructions over the Arctic on October 29 and 30, 2003. (a, b) TEC maps, the color scale is from 0 to 60 TECU. (c, d) The cross-sections cut the ionosphere along the lines indicated on the TEC maps, x is the distance on Earth's surface along highlighted lines and h is the height, the color scale is from 0 до  $2.5 \cdot 10^{12} \text{ m}^{-3}$ .

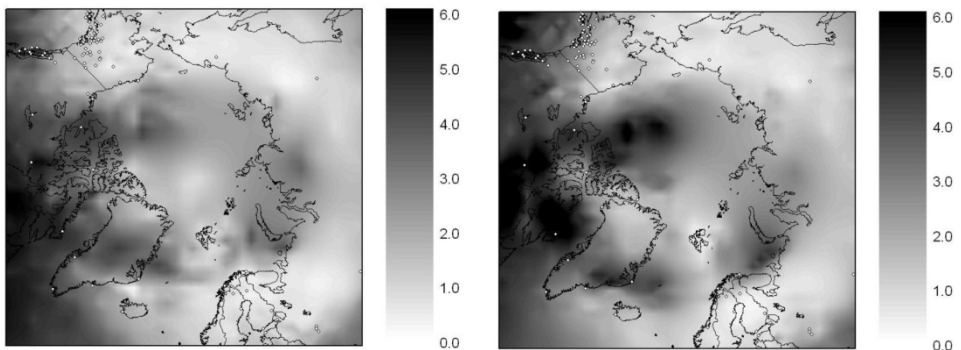


**Figure 20.** Vertical TEC in Arctic according to HORT on December 16, 2006 at 18:00 UT (left) and 19:00 UT (right)

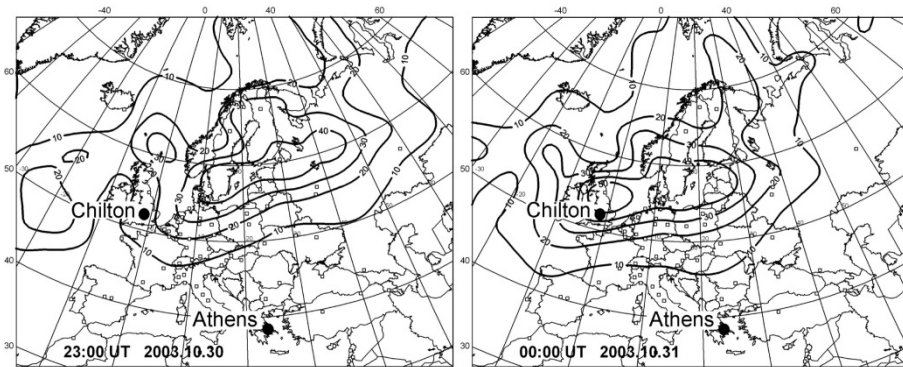


**Figure 21.** Contours of vertical TEC over European region on 30 October, 2003 at 23:00 UT (left) and at 24:00 UT (right)

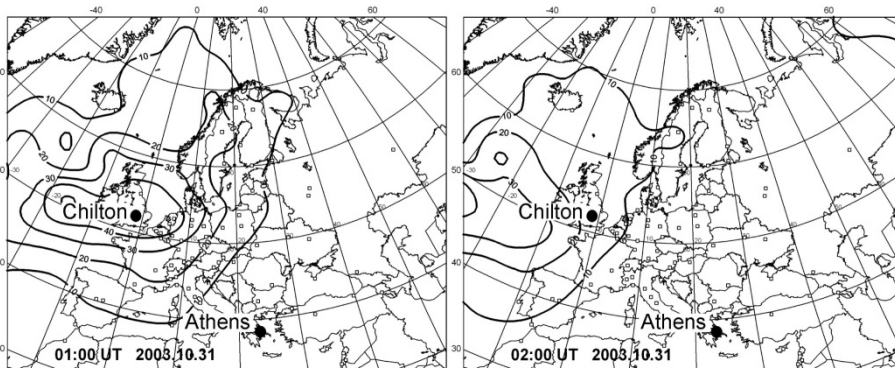


**Figure 22.** Contours of vertical TEC over European region on 31 October, 2003 at 01:00 UT (left) and at 02:00 UT (right)

The TOI observed on October 30, 2003, whose further evolution as the plasma moved above the northern Europe was traced in [46] from the LORT and HORT data and the European ionosonde measurements, is also analyzed in a number of other works. Mitchell et al. [47] compare the signatures of TOI that were observed on October 30, 2003 in the TEC distributions calculated by MIDAS GPS RT tool with the amplitude and phase fluctuations of the GPS signal recorded by the specialized receiver on Svalbard. Increased TEC (up to 70 TECU) is observed from 21:00 to 21:30 in a band north of and across Scandinavia towards Greenland at above 70°N.

Ionospheric disturbances above Japan after the strongest Tohoku earthquake were analyzed by HORT methods with very high time resolution (2-3 minutes, a result of the 1200 ground stations in Japan) in [48]. The disturbances observed in the vertical TEC an hour after the main

shock are shown in Figure 24. The TEC waves induced by the earthquake-generated AGWs are seen propagating outwards from the epicentral area. The spatial limits of the diagram correspond to the limited area within which the receiving network is sufficiently dense.

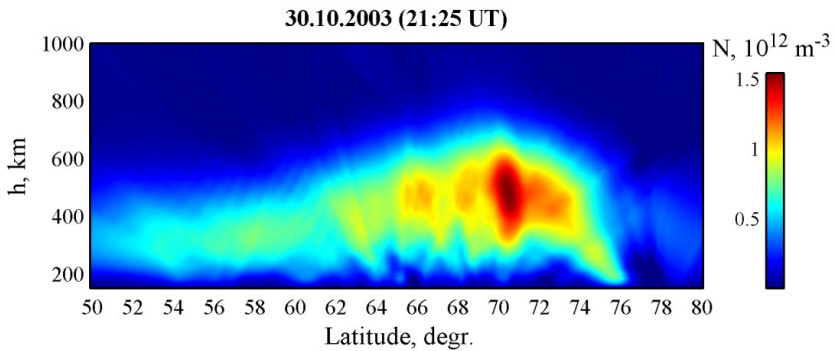


**Figure 23.** LORT image of the ionosphere (Moscow-Svalbard) on October 30, 2003 at 21:25 UT

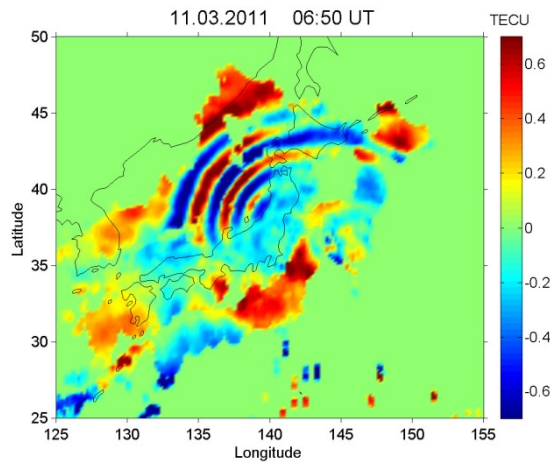


**Figure 24.** The diverging disturbance caused by the acoustic gravity waves generated by the Tohoku earthquake

We note that GPS/GLONASS-based remote sounding and HORT are being extensively developed and used in new practical applications [49-53].

## 5. Combination with other sounding techniques

Existing systems (FormoSat-3/COSMIC and a few others are capable of recording GNSS signals onboard low-Earth orbiting satellite platforms). These satellites effectively demonstrate the radio occultation technique (OT) which acquires quasi-tangential projections of electron density  $N$  [54-56]. The OT method, coupled with subsequent ground reception of the OT data, opens up the possibility of sounding the ionosphere in a wide range of different geometries of the transmitting and receiving systems. The OT method provides integrals of  $N$  over a set of quasi-tangential rays (the satellite-satellite links), and is a particular case of the RT method. It is, however, necessary to construct a procedure for synthesizing the occultation data into the general RT process [7, 8, 57]. The combination of RT and OT, when the RT data are supplemented by the satellite-to-satellite sounding (OT) data, would noticeably improve the vertical resolution of the RT reconstructions.

Existing ultra-violet (UV)-sounding systems (GUVI, SSULI, FormoSat-3/COSMIC) provide integrals of  $N$  squared. UV sounding data can be incorporated into the general tomographic iterative scheme. For example, at the first step of a reconstruction, the main iteration is accomplished with linear integrals and RT data alone. Then, based on the distribution of electron density  $N$  obtained in the first iteration, we run the iterative scheme for  $N$  squared with the UV input. Third, we transform the distribution of  $N$  squared derived at this step of the reconstruction into the distribution of  $N$  (the result of the second iteration); since this distribution can be used further. Thus, the odd iterations will work with the radio sounding data, while even iterations will use UV input. Overall, we obtain a tomographic methodology which uses both radio sounding and UV sounding data. However, in order to ensure convergence and to obtain high-quality final results, the experimental data of different kinds should be consistent and have commensurate accuracy, otherwise the additional iterations based on the "bad" data will degrade the result. Unfortunately, as of now, the UV data are far less accurate than the navigation radio sounding data.

Note that the RT methods described here refer to "ray" tomography [1] that neglects diffraction effects. In previous work, we developed methods for diffraction tomography and statistical tomography [1, 2, 4, 7]. Diffraction tomography is applicable for imaging the structure of isolated localized irregularities with allowance for diffraction effects. Statistical tomography reconstructs the spatial distributions of the statistical parameters of the randomly irregular ionosphere [7, 58].

## 6. Conclusions

This Chapter briefly outlines the results of tomographic studies of the ionosphere conducted with the participation of the authors. The methods applied in satellite radio tomography of the near-Earth plasma, including LORT and HORT, are described. During the last two decades, numerous RT experiments, studying the equatorial, mid-latitude, sub-auroral, and auroral ionosphere were carried out in different regions of the world (in Europe, USA, and Southeast

Asia). Examples of RT images of the ionospheric electron density based on data recorded in a series of RT experiments have been presented.

An RT system is a distributed sounding system: the moving satellites with onboard transmitters and receivers together with the ground receiving networks enable continuous sounding of the medium along different directions and support imaging of the spatial structure of the ionosphere. Satellite RT, utilizing a system of ground and satellite receivers, combined with traditional means of ionospheric sounding provides the basis for regional and global monitoring of the near-Earth plasma.

## Acknowledgements

We are grateful to professors L.-C. Tsai and C.H. Liu, our colleagues from the Center for Space and Remote Sensing Research (National Central University, Chungli, Taiwan), and the University of Illinois at Urbana Champaign for providing experimental data. We acknowledge use of the worldwide ionosonde database accessed from the National Geophysical Data Center (NGDC) and Space Physics Interactive Data Resource (SPIDR). The authors are grateful to North-West Research Associates (NWRA) for providing experimental relative TEC data in the Alaska region. This work was supported by the Russian Foundation for Basic Research (grants 13-05-01122, 11-05-01157), the Ministry for Education and Science of the Russian Federation (project 14.740.11.0203), a grant of the President of Russian Federation (project MK-2544.2012.5), and M.V. Lomonosov Moscow State University Development Programme.

## Author details

Vyacheslav Kunitsyn\*, Elena Andreeva, Ivan Nesterov and Artem Padokhin

\*Address all correspondence to: [kunitsyn@phys.msu.ru](mailto:kunitsyn@phys.msu.ru)

M. Lomonosov Moscow State University, Faculty of Physics, Moscow, Russia

## References

- [1] Kunitsyn, V. E, & Tereshchenko, E. D. Tomography of the Ionosphere. Moscow: Nauka; (1991). (In Russian).
- [2] Kunitsyn, V. E, & Tereshchenko, E. D. Radiotomography of the Ionosphere. IEEE Antennas and Propagation Magazine (1992). 34, 22-32.
- [3] Leitinger, R. Ionospheric tomography. In: Stone R. (ed.) Review of Radio Science 1996-1999. Oxford: Science Publications; (1999). p.581-623.

- [4] Kunitsyn, V. E, & Tereshchenko, E. D. *Ionospheric Tomography*. Berlin, NY: Springer; (2003).
- [5] Pryse, S. E. Radio Tomography: A new experimental technique. *Surveys in Geophysics* (2003). 24, 1-38.
- [6] Bust, G. S, & Mitchell, C. N. History, current state, and future directions of ionospheric imaging. *Reviews of Geophysics* (2008). 46, RG1003, doi: 10.1029/2006RG000212
- [7] Kunitsyn, V. E, Tereshchenko, E. D, & Andreeva, E. S. *Radio Tomography of the Ionosphere*. Moscow: Nauka; (2007). (In Russian).
- [8] Kunitsyn, V. E, Tereshchenko, E. D, Andreeva, E. S, & Nesterov, I. A. Satellite radio probing and radio tomography of the ionosphere. *Uspekhi Fizicheskikh Nauk* (2010). 180(5), 548-553.
- [9] Andreeva, E. S, Kunitsyn, V. E, & Tereshchenko, E. D. Phase difference radiotomography of the ionosphere. *Annales Geophysicae* (1992). 10, 849-855.
- [10] Kunitsyn, V. E, Andreeva, E. S, Kozharin, M. A, & Nesterov, I. A. Ionosphere Radio Tomography using high-orbit navigation system. *Moscow University Physics Bulletin* (2005). 60(1), 94-108.
- [11] Hofmann-Wellenhof, B, Lichtenegger, H, & Collins, J. *Global Positioning System: theory and practice*. Berlin, NY: Springer; (1992).
- [12] Kunitsyn, V. E, Kozharin, M. A, Nesterov, I. A, & Kozlova, M. O. Manifestations of helio-geophysical disturbances in October, 2003 in the ionosphere over West Europe from GNSS data and ionosonde measurements. *Moscow University Physics Bulletin* (2004). 59(6), 68-71.
- [13] Kersley, L, Heaton, J, Pryse, S, & Raymund, T. Experimental ionospheric tomography with ionosonde input and EISCAT verification. *Annales Geophysicae* (1993). 11, 1064-1074.
- [14] Kunitsyn, V. E, Andreeva, E. S, Razinkov, O. G, & Tereschhenko, E. D. Phase and phase-difference ionospheric radiotomography. *International Journal of Imaging Systems and Technology* (1994). 5(2), 128-140.
- [15] Heaton, J, Pryse, S, & Kersley, L. Improved background representation, ionosonde input and independent verification in experimental ionospheric tomography. *Annales Geophysicae* (1995). 13, 1297-1302.
- [16] Heaton, J, Jones, G, & Kersley, L. Toward ionospheric tomography in Antarctica: First steps and comparison with dynasonde observations. *Antarctic Science* (1996). 8, 297-302.

- [17] Heaton, J, Cannon, P, Rogers, N, Mitchell, C, & Kersley, L. Validation of electron density profiles derived from oblique ionograms over the United Kingdom. *Radio Science* (2001). 36, 1149-1156.
- [18] Dabas, R, & Kersley, L. Radio tomographic imaging as an aid to modeling of ionospheric electron density. *Radio Science* (2003). 38(3), doi:10.1029/2001RS002514.
- [19] Franke, S. J, Yeh, K. C, Andreeva, E. S, & Kunitsyn, V. E. A study of the equatorial anomaly ionosphere using tomographic images. *Radio Science* (2003). 38(1), doi: 10.1029/2002RS002657.
- [20] Yeh, K. C, & Liu, C. H. *Theory of Ionospheric Waves*. New York: Academic Press; (1972).
- [21] Pryse, S, & Kersley, L. A preliminary experimental test of ionospheric tomography. *Journal of Atmospheric and Terrestrial Physics* (1992). 54, 1007-1012.
- [22] Raymund, T, Pryse, S, Kersley, L, & Heaton, J. Tomographic reconstruction of ionospheric electron density with European incoherent scatter radar verification. *Radio Science* (1993). 28, 811-817.
- [23] Kersley, L, Heaton, J, Pryse, S, & Raymund, T. Experimental ionospheric tomography with ionosonde input and EISCAT verification. *Annales Geophysicae* (1993). 11, 1064-1074.
- [24] Foster, J, Buonsanto, M, Holt, J, Klobuchar, J, Fougere, P, Pakula, W, Raymund, T, Kunitsyn, V. E, Andreeva, E. S, Tereshchenko, E. D, & Khudukon, B. Z. Russian-American Tomography Experiment. *International Journal of Imaging Systems and Technology* (1994). 5, 148-159.
- [25] Pakula, W, Fougere, P, Klobuchar, L, Kuenzler, H, Buonsanto, M, Roth, J, Foster, J, & Sheehan, R. Tomographic reconstruction of the ionosphere over North America with comparisons to ground-based radar. *Radio Science* (1995). 30(1), 89-103.
- [26] Walker, I, Heaton, J, Kersley, L, Mitchell, C, Pryse, S, & Williams, M. EISCAT verification in the development of ionospheric tomography. *Annales Geophysicae* (1996). 14, 1413-1421.
- [27] Nygren, T, Markkanen, M, Lehtinen, M, Tereshchenko, E, Khudukon, B, Evstafiev, O, & Pollari, P. Comparison of F-region electron density observations by satellite radio tomography and incoherent scatter methods. *Annales Geophysicae* (1996). 14, 1422-1428.
- [28] Spenser, P, Kersley, L, & Pryse, S. A new solution to the problem of ionospheric tomography using quadratic programming. *Radio Science* (1998). 33(3), 607-616.
- [29] Foster, J, & Rich, F. Prompt mid-latitude electric field effects during severe geomagnetic storm. *Journal of Geophysical Research* (1998). 103(11), 26367-26372.

- [30] Raymund, T, Bresler, Y, Anderson, D, & Daniell, R. Model-assisted ionospheric tomography: A new algorithm. *Radio Science* (1994). 29, 1493-1512.
- [31] Kunitsyn, V, Nesterov, I, Padokhin, A, & Tumanova, Y. Ionospheric Radio Tomography Based on the GPS/GLONASS Navigation Systems. *Journal of Communications Technology and Electronics* (2011). 56(11), 1269-1281.
- [32] Andreeva, E. S, Galinov, A. V, Kunitsyn, V. E, Mel'nichenko, Yu. A, Tereshchenko E. D, Filimonov M. A, & Chernyakov, S. M. Radio tomographic reconstruction of ionisation dip in the plasma near the Earth. *Journal of Experimental and Theoretical Physics Letters* (1990). 52, 145-148.
- [33] Oraevsky, V. N, Rushin, Yu. Ya, Kunitsyn, V. E, Razinkov, O. G, Andreeva, E. S, Depueva, A. Kh, Kozlov, E. F, & Shagimuratov, I. I. Radiotomographic cross-sections of the subauroral ionosphere along trace Moscow-Arkhangelsk. *Geomagnetism and Aeronomy* (1995). 35(1), 117-122.
- [34] Cook, J, & Close, S. An investigation of TID evolution observed in MACE'93 data. *Annales Geophysicae* (1995). 13, 1320-1324.
- [35] Andreeva, E. S, Franke, S. J, Yeh, K. C, & Kunitsyn, V. E. Some features of the equatorial anomaly revealed by ionospheric tomography. *Geophysical Research Letters* (2000). 27, 2465-2458.
- [36] Yeh, K. C, Franke, S. J, Andreeva, E. S, & Kunitsyn, V. E. An investigation of motions of the equatorial anomaly crest. *Geophysical Research Letters* (2001). 28, 4517-4520.
- [37] Andreeva, E. S. Possibility to reconstruct the ionosphere E and D regions using ray radio tomography. *Moscow University Physics Bulletin* (2004). 59(2), 67-75.
- [38] Kunitsyn, V. E, Tereshchenko, E. D, Andreeva, E. S, Grigor'ev, V. F, Romanova, N. Yu, Nazarenko, M. O, Vapiro, Yu. M, & Ivanov, I. I. Transcontinental Radio Tomographic Chain: First Results of Ionospheric Imaging. *Moscow University Physics Bulletin* (2009). 64(6), 661-663.
- [39] Ahmadov, R, & Kunitsyn, V. Simulation of generation and propagation of acoustic gravity waves in the atmosphere during a rocket flight. *International Journal of Geomagnetism and aeronomy* (2004). 5(2), 1-12, doi:10.1029/2004GI000064.
- [40] Andreeva, E. S, Gokhberg, M. B, Kunitsyn, V. E, Tereshchenko, E. D, Khudukon, B. Z, & Shalimov, S. L. Radiotomographical detection of ionosphere disturbances caused by ground explosions. *Cosmic Research* (2001). 39(1), 13-17.
- [41] Kunitsyn, V. E, Andreeva, E. S, Frolov, V. L, Komrakov, G. P, Nazarenko, M. O, & Padokhin, A. M. Sounding of HF heating-induced artificial ionospheric disturbances by navigational satellite radio transmissions. *Radio Science* (2012). RS0L15, doi: 10.1029/2011RS004957.

- [42] Kunitsyn, V. E, Andreeva, E. S, Franke, S. J, & Yeh, K. C. Tomographic investigations of temporal variations of the ionospheric electron density and the implied fluxes. *Geophysical Research Letters* (2003). 30(16), doi:10.1029/2003GL016908
- [43] Kunitsyn, V. E, & Nesterov, I. A. GNSS radio tomography of the ionosphere: The problem with essentially incomplete data. *Advances in Space Research* (2011). 47, 1789-1803.
- [44] Kulchitsky, A, Maurits, S, Watkins, B, et al. Drift simulation in an Eulerian ionospheric model using the total variation diminishing numerical scheme. *Journal of Geophysical Research* (2005). 110, 1-14. A09310, doi:10.1029/2005JA011033
- [45] Foster, J. C, Coster, A. J, Erickson, P. J, Holt, J. M, Lind, F. D, Rideout, W, McCreedy, M, Van Eyken, A, Barnes, R. J, Greenwald, A, & Rich, F. J. Multiradar observations of the polar tongue of ionization. *Journal of Geophysical Research* (2005). 110, A09S31, doi:10.1029/2004JA010928.
- [46] Kunitsyn, V. E, Kozharin, M. A, Nesterov, I. A, & Kozlova, M. O. Manifestations of heliospheric disturbances of October 2003 in the ionosphere over Western Europe according to the data of GNSS tomography and ionosonde measurements. *Moscow University Physics Bulletin* (2004). 6, 67-69.
- [47] Mitchell, C, Alfonsi, L, De Franceschi, G, Lester, M, Romano, V, & Wernik, A. GPS TEC and scintillation measurements from the polar ionosphere during the October 2003 storm. *Geophysical Research Letters* (2005). 32, L12S03, doi: 10.1029/2004GL021644.
- [48] Kunitsyn, V, Nesterov, I, & Shalimov, S. Japan Earthquake on March 11, 2011: GPS-TEC Evidence for Ionospheric Disturbances. *Journal of Experimental and Theoretical Physics Letters* (2011). 94(8), 616-620.
- [49] Ma, X. F, Maruyama, T, Ma, G, & Takeda, T. Three-dimensional ionospheric tomography using observation data of GPS ground receivers and ionosonde by neural network. *Journal of Geophysical Research* (2005). 110, A05308, doi: 10.1029/2004JA010797.
- [50] Jin, S. G, & Park, J. U. GPS ionospheric tomography: a comparison with the IRI-2001 model over South Korea. *Earth Planets Space* (2007). 59(4), 287-292.
- [51] Zhao, H. S, Xu, Z. W, Wu, J, & Wang, Z. G. Ionospheric tomography by combining vertical and oblique sounding data with TEC retrieved from a tri-band beacon. *Journal of Geophysical Research* (2010). 115, A10303, doi:10.1029/2010JA015285.
- [52] Jin, S. G, Feng, G. P, & Gleason, S. Remote sensing using GNSS signals: Current status and future directions. *Advances in Space Research* (2011). 47, 1645-1653.
- [53] Jin, S. G. GNSS Atmospheric and Ionospheric Sounding. In: Jin SG (ed.) *Global Navigation Satellite Systems- Signal, Theory and Application*. Rijeka: InTech; (2012). p. 359-381.

- [54] Hajj, G, Ibanez-meier, R, Kursinski, E, & Romans, L. Imaging the ionosphere with the global positioning system. *International Journal of Imaging Systems and Technology* (1994). 5(2), 174-187.
- [55] Kursinski, E, Hajj, G, Beritger, W, et al. Initial results of radio occultation of Earth atmosphere using GPS. *Science* (1996). 271(5252), 1107-1110.
- [56] Liou, Y. A, Pavelyev, A. G, Matyugov, S. S, et al. *Radio Occultation Method for Remote Sensing of the Atmosphere and Ionosphere*. Ed. Y.A. Liou. Rijeka: InTech; (2010)
- [57] Andreeva, E. S, Berbeneva, N. A, & Kunitsyn, V. E. Radio tomography using quasi tangential radiosounding on traces satellite-satellite. *Geomagnetism and Aeronomy* (1999). 39(6), 109-114.
- [58] Tereschenko, E. D, Kozlova, M. O, Kunitsyn, V. E, & Andreeva, E. S. Statistical tomography of subkilometer irregularities in the high-latitude ionosphere. *Radio Science* (2004). 39, RS1S35, doi:10.1029/2002RS002829.